DIFFERENTIAL SHIFT ESTIMATION IN THE ABSENCE OF COHERENCE: PERFORMANCE ANALYSIS AND BENEFITS OF POLARIMETRY

Michelangelo Villano[(1)], Konstantinos P. Papathanassiou[(1)]

[(1)]German Aerospace Center (DLR), Microwaves and Radar Institute,
Muenchner Str. 20, 82234 Wessling, Germany, Email: michelangelo.villano@dlr.de

ABSTRACT

The estimation of the local differential shift between synthetic aperture radar (SAR) images has proven to be an effective technique for monitoring glacier surface motion. As images acquired over glaciers by short wavelength SAR systems, such as TerraSAR-X, often suffer from a lack of coherence, image features have to be exploited for the shift estimation (feature-tracking).
The present paper addresses feature-tracking with special attention to the feasibility requirements and the achievable accuracy of the shift estimation. In particular, the dependence of the performance on image characteristics, such as texture parameters, signal-to-noise ratio (SNR) and resolution, as well as on processing techniques (despeckling, normalised cross-correlation versus maximum likelihood estimation) is analysed by means of Monte-Carlo simulations. TerraSAR-X data acquired over the Helheim glacier, Greenland, and the Aletsch glacier, Switzerland, have been processed to validate the simulation results.
Feature-tracking can benefit of the availability of fully-polarimetric data. As some image characteristics, in fact, are polarisation-dependent, the selection of an optimum polarisation leads to improved performance. Furthermore, fully-polarimetric SAR images can be despeckled without degrading the resolution, so that additional (smaller-scale) features can be exploited.

1. INTRODUCTION

Synthetic aperture radar (SAR) represents a useful tool for monitoring flowing glaciers. In particular, the estimation of the glacier surface velocity can be accomplished by acquiring SAR images of the areas of interest at regular intervals and estimating the local differential shift between pairs of images [1].
In case the two SAR images are characterized by partial coherence, the differential shift can be retrieved by means of coherent cross-correlation or incoherent cross-correlation (speckle-tracking) [2]. An analytical derivation of the accuracy of the differential shift estimation for coherent cross-correlation is given in [3].
In the absence of coherence between the two SAR images, the differential shift can only be retrieved by exploiting the features of the SAR images, when present (feature-tracking). The speckle patterns of the two SAR images, in fact, are no longer correlated and cannot be used for the shift estimation.
In order to address feature-tracking, a statistical characterisation of the SAR images is required. This is discussed in section 2, where it is also shown how to generate simulated images and estimate the parameters of the model from data. The processing to be performed is presented in section 3, where the processing parameters are highlighted.
The feasibility of feature-tracking and its dependence on image and processing parameters is then addressed in section 4, while the accuracy of the shift estimation is analysed in section 5. Monte-Carlo simulations are widely used to assess both the feasibility and the performance.
The benefits of polarimetry are considered in section 6, while some conclusions are drawn in section 7.

2. STATISTICAL CHARACTERIZATION OF THE SAR IMAGES

2.1. Modelling the Two SAR Images

Each complex SAR image $u[k,h]$ can be characterized according to the product model [4] by the product of the square root of an underlying radar cross section (RCS) $\sigma[k,h]$ and a complex speckle pattern $n[k,h]$, to which the thermal noise contribution $t[k,h]$ adds:

$$u[k,h] = \sqrt{\sigma[k,h]}n[k,h] + t[k,h] \quad (1)$$

The RCS, the speckle pattern, and the thermal noise contribution are intended as realizations of statistical processes. The statistical process concerning the RCS can be in general characterized by a gamma probability density function (PDF), for which the mean value $<\sigma>$ and the order parameter ν are to be specified, and by a Gaussian auto-correlation function (ACF), whose range and azimuth correlation lengths, l_{rg} and l_{az}, are to be specified. The speckle process can be characterized by a zero-mean complex Gaussian PDF with unitary variance and is spatially uncorrelated. The ACF of the speckle process, in fact, is given by the autocorrelation of the point spread function (PSF), therefore the speckle is correlated only within the resolution cell, and speckle realisations corresponding to different, even adjacent, resolution cells are uncorrelated [5]. The thermal noise contribution $t[k,h]$ is modelled as additive white Gaussian noise and is characterized by the signal-to-noise ratio (SNR) *SNR*.

Proc. 'PolInSAR 5th Int. Workshop on Science and Applications of SAR Polarimetry and Polarimetric Interferometry', Frascati, Italy, 24–28 January 2011 (ESA SP-695, March 2011)

As far as the estimation of the shift field is concerned, two SAR images, $u_1[k,h]$ and $u_2[k,h]$, are assumed to be available, characterized according to the described model and such that their speckle patterns are uncorrelated, while their underlying RCS are related by means of a two-dimensional displacement field ($\Delta_{rg}[k,h]$, $\Delta_{az}[k,h]$):

$$\begin{aligned} u_1[k,h] &= \sqrt{\sigma[k,h]}n_1[k,h] + t_1[k,h] \\ u_2[k,h] &= \sqrt{\sigma[k+\Delta_{rg}[k,h], h+\Delta_{az}[k,h]]}n_2[k,h] + t_1[k,h] \\ E\{n_1[k,h]n_2[k,h]\} &= 0 \end{aligned} \quad (2)$$

In effect, as the SAR image can be assumed to be known but for a multiplicative constant, one of the mentioned image parameters, namely the mean value of the gamma PDF, is not required for our analysis.
The range and correlation lengths are to be specified in units of resolution cells and so will the estimation accuracy be expressed as well. That is also the reason why range and azimuth resolutions are not specified among the above listed parameters.

2.2. Generation of Correlated K-Distributed Images

Simulated SAR images, statistically characterised according to the described model, can be obtained by independently generating the underlying RCS and the speckle pattern. Several methods to generate correlated gamma distributed RCS two-dimensional trends are reviewed in [6]. Among them, the technique described in [7] is chosen.

2.3. Estimation of Texture Parameters from Data

The mean value and the order parameter of the gamma PDF and the range and azimuth correlation lengths of the Gaussian ACF are often referred to as texture parameters and can be estimated from data.
When estimating these parameters, it has to be considered that they refer to the underlying RCS, while we only have at our disposal the intensity image. The mean value of the underlying RCS is equal to the mean value of the intensity image and can be therefore estimated by taking the mean intensity over a given area. The estimation of the order parameter of the underlying RCS ν, which is defined as the ratio of the RCS variance to the squared RCS mean, instead can be rather accurately estimated with a technique based on the normalised log statistics [8]. In particular, the order parameter can be obtained by inverting the following equation:

$$\langle \ln(I) \rangle - \ln(\langle I \rangle) = \psi^{(0)}(\nu) - \ln(\nu) - \gamma_E \quad (3)$$

where $\psi^{(0)}$ is the digamma function and γ_E is the Euler-Mascheroni constant. Low values of the order parameter (high values of the image contrast) denote the presence of well-defined features in a given image area. Fig. 1 shows the estimated order parameter for a TerraSAR-X image, acquired over the Helheim glacier, Greenland. It may be noticed that the crevasse areas of the glaciers are rich in features and are therefore characterised by a low order parameter.

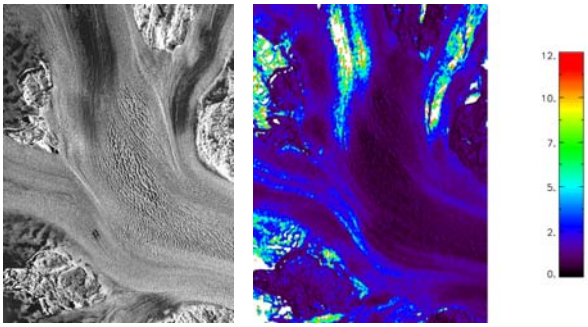

Figure 1. Estimated order parameter for a TerraSAR-X image acquired over the Helheim glacier, Greenland

The correlation lengths can be estimated directly on the despeckled intensity image.

3. PROCESSING STAGES

In the absence of coherence, the retrieval of the local differential shift between two SAR images can be divided into two stages:
1) A pre-processing of the complex SAR images, $u_1[k,h]$ and $u_2[k,h]$, whose output is the couple of real-valued images, $A_1[k,h]$ and $A_2[k,h]$, to be used for the differential shift estimation. This typically includes square detection and despeckling of the SAR images.
Despeckling can be performed by smoothing the intensity image, using a rectangular N_{Lrg} X N_{Laz} window. This technique, referred to as multilook despeckling, is the MLE estimation of the RCS in case all the pixels within the window are characterized by the same RCS [3];
2) The estimation of the local differential shifts, whose input is the couple of real-valued images obtained in the first stage. A template of N pixels, also referred to as patch, is extracted from the first image (reference patch) and compared with different candidate patches, extracted from the second image, on the basis of a measure of similarity. In particular, a similarity function $S[\Delta_{rg}, \Delta_{az}]$ may be defined. Rectangular patches of N_{rg} X N_{az} pixels ($N = N_{rg}\ N_{az}$) are usually employed. The patch of the second image, for which the similarity function is maximum, is selected as the matching patch. The estimated differential shift is given by the difference of the coordinates of the matching and reference patches. Two similarity functions, which can be employed, are:

- *Normalized cross-correlation* (NCC), defined as:

$$S_{NCC}[\Delta_{rg},\Delta_{az}]=\frac{\sum_{k=k_c-\frac{N_{rg}}{2}}^{k_c+\frac{N_{rg}}{2}-1}\sum_{h=h_c-\frac{N_{az}}{2}}^{h_c+\frac{N_{az}}{2}-1}\left(A_1[k,h]-m_1\right)\left(A_2[k+\Delta_{rg},h+\Delta_{az}]-m_2\right)}{\sigma_1\sigma_2} \quad (4)$$

where m_1, m_2, σ_1, and σ_2 are the averages and the standard deviations of the pixels included in the patches extracted from A_1 and A_2.

- *Maximum Likelihood* (ML), proposed in [9] and defined as:

$$S_{ML}[\Delta_{rg},\Delta_{az}]=\sum_{k=k_c-\frac{N_{rg}}{2}}^{k_c+\frac{N_{rg}}{2}-1}\sum_{h=h_c-\frac{N_{az}}{2}}^{h_c+\frac{N_{az}}{2}-1}\left[\ln(LR)-2\ln(1+LR)\right] \quad (5)$$

where

$$LR=\frac{A_1[k,h]}{A_2[k+\Delta_{rg},h+\Delta_{az}]} \quad (6)$$

In principle, the latter measure of similarity should lead to a better accuracy compared to the previous one, because it is derived by taking into account the first order statistical properties of the SAR images. However, in its derivation, the underlying RCS is assumed to be uncorrelated.

The local differential shift is not necessarily an integer number of resolution cells, but it is in general fractional. In order to estimate this fractional shift, SAR images can be oversampled, preferably before square detection and despeckling. The oversampling of the images seriously affects the computational cost and the processing times. As an alternative, it is possible to oversample the two-dimensional similarity function, assuming for it a regular trend in the vicinity of the peak.

4. FEASIBILITY

4.1. A Criterion for Feasibility

With reference to the processing steps described in section 3, for an unambiguous estimation, it is necessary that the value of the similarity function between the reference patch and the matching patch $S_{matching}$ is higher than the value of similarity function between the reference patch and all other candidate patches $S_{non\_matching\ j}$:

$$S_{matching} > S_{non\_matching\ j}, \forall j \quad (7)$$

Having characterised SAR images as realisations of statistical processes, the quantities $S_{matching}$ and $S_{non\_matching\ j}$ can also be interpreted as realisations of random variables, statistically characterised by the PDFs $p_{S\ matching}(S_{matching})$ and $p_{S\ non\_matching}(S_{non\_matching})$ respectively. These PDFs depend on image parameters (order parameter, correlation lengths, SNR), as well as on processing parameters (despeckling options, size of the patch, similarity function to be used for the estimation) and can be estimated by using simulated textures, generated as explained in subsection 2.2. Matching patches are characterised by the same underlying RCS and by different uncorrelated speckle patterns, while non-matching patches are characterised by different underlying RCS (but realisations of the same statistical process) and different uncorrelated speckle patterns. An example of such PDFs for a given set of parameters is shown in Fig. 2, where NCC has been used as a similarity function.

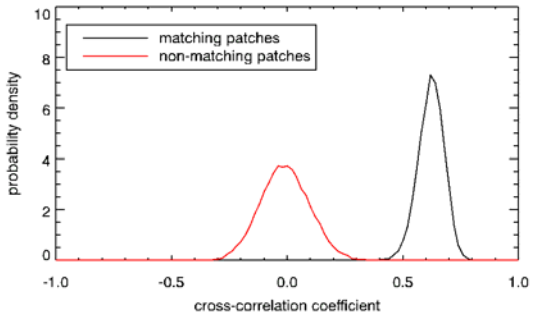

Figure 2. PDFs of the cross-correlation coefficient for matching and non-matching patches

A feasibility criterion can therefore be defined with reference to these PDFs in the sense that in order for the shift estimation to be unambiguous the two PDFs must not overlap. From a statistical point of view, the "bounds" of a PDF can be identified using occurrence levels, imposing that $S_{matching\ a\%}$ (with *a%* slightly smaller than 100%) is greater than $S_{matching\ b\%}$ (with *b%* slightly bigger than 0%):

$$S_{matching\ a\%} > S_{non\_matching\ b\%} \quad (8)$$

The occurrence levels *a%* and *b%* cannot be fixed *a priori*, because they are related to the number of candidate patches, which may vary. A feasibility value *f* can be defined as the difference of the two mentioned quantities, such that a positive value of *f* corresponds to feasibility:

$$f = S_{matching\ a\%} - S_{non\_matching\ b\%} \quad (9)$$

4.2. Requirements for Feasibility

The feasibility value f depends on the image and processing parameters. When expressed as a function of all these parameters, the feasibility value f can be referred to as the feasibility function.

The feasibility function divides the space of parameters into two regions, namely the region for which $f > 0$ and the complementary one. The aim of the feasibility analysis is to determine the boundary of the two regions. In effect, some of the parameters of the feasibility function, namely $N_{L\ rg}$ and $N_{L\ az}$ (despeckling window size) are related to the processing and can be therefore arbitrarily selected. In particular, they can be selected to maximise the feasibility function and an optimised feasibility function f_{opt} no longer dependent on the despeckling window size can be defined. The size of the patch (N_{rg} X N_{az}) could appear as a parameter which can be arbitrarily selected, but, in practice, it has to be chosen such that the shift is uniform within the patch. In particular, the difference between the range/azimuth shifts for two different resolution cells within the patch should never exceed the range/azimuth correlation lengths. The maximum size of the patch is therefore related to the velocity field itself and its implications for the mission design, such as the requirement in terms of maximum temporal baseline, are considered in detail in subsection 4.3.

The similarity function can be arbitrarily selected, but it is not possible to compare values of feasibility functions obtained with different similarity function, e.g. if the value of the feasibility function for a given set of parameters using NCC is 0.3, while the value of the feasibility function for the same set of parameters using ML is 0.05, it is only possible to conclude that in both cases the technique is feasible. A similarity function A can be selected as more suitable than a feasibility function B, according to the feasibility criterion, if the region for which $f > 0$, obtained by using the similarity function A, contains the region for which $f > 0$, obtained by using the similarity function B.

The optimum despeckling options are in general dependent on texture parameters and can be different for the two similarity functions. Fig. 3 and Fig. 4 show the trends of the feasibility function as a function of the size of the despeckling window size $N_L = N_{Lrg}\ N_{Laz}$ for different values of the order parameter and correlation length respectively, using NCC. It can be noticed that the optimum despeckling window size does not depend on the order parameter. A slight dependence of the optimum despeckling window size on the correlation length can instead be observed: the larger the correlation length, the larger the optimum despeckling window size. The larger is the correlation length, in fact, the greater is the number of neighbouring pixels with the same or very similar RCS. In this case, despeckling using relatively large windows leads to a removal of the speckle and a preservation of the underlying RCS trend, as it is rather constant within the despeckling window. In contrast, despeckling images with smaller correlation length using relatively large windows leads to a deterioration of the underlying RCS trend, as the averaging is performed over areas with different values of the underlying RCS.

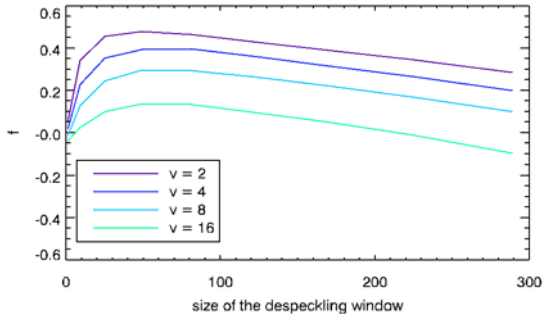

Figure 3. Feasibility function vs. size of the despeckling window size for different order parameters

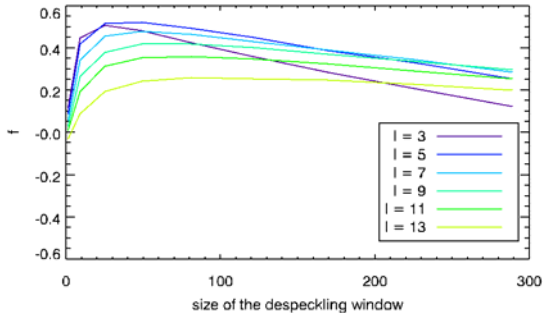

Figure 4. Feasibility function vs. size of the despeckling window size for different correlation lengths

As apparent from the plots, in the absence of coherence, despeckling the intensity images before correlating the image patches is of advantage. If the estimation of the differential shift is carried out without despeckling the images, a large number of wrong estimates will be present in the resulting shift maps, as shown in Fig. 5, where shift maps of the Helheim glacier, Greenland, have been computed with (7 X 7 window) and without despeckling. It is apparent that the number of wrong estimates is by far higher in the shift maps obtained without performing despeckling.

Once the despeckling options have been fixed accordingly to the carried out analysis, the optimised feasibility function f_{opt} as a function of the texture characteristics is obtained. In particular, in the special case of equal range and azimuth correlation lengths, the two-dimensional trend of such a function can be displayed. In particular, from the previous analysis, it seems reasonable to optimise the feasibility function,

using a window size of 7 X 7 pixels in case of NCC and of 3 X 3 pixels in case of ML.

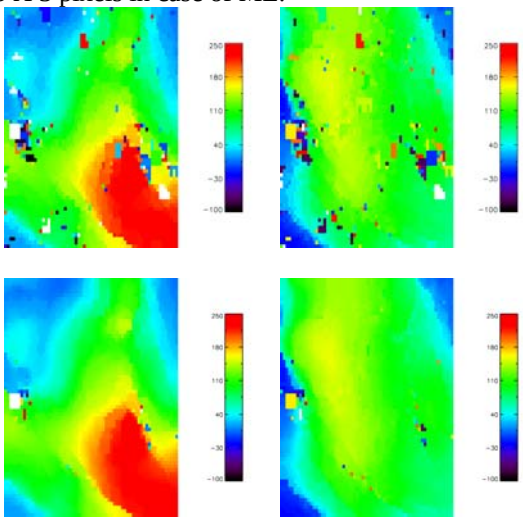

Figure 5. Shift maps from the Helheim glacier, obtained with (bottom) and without (top) despeckling

What we are interest in, more than the trend of the feasibility function, is indeed the boundary between the feasibility and the non-feasibility regions. Fig. 6 shows this boundary, for both NCC and ML, using 64 X 64 pixel patches.

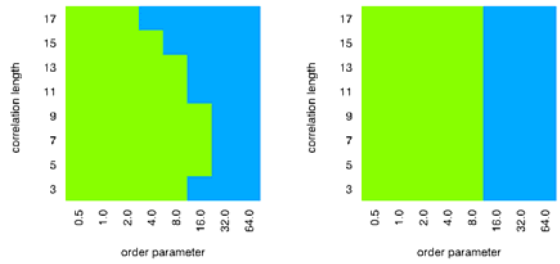

Figure 6. Feasibility (green) and non-feasibility (blue) regions for NCC (left) and ML (right)

A minimum value of the order parameter is required. As lower order parameters denote image areas with well-defined features, this is equivalent to require the presence of features.

Fig. 7 includes some shift maps from the Aletsch glacier, Switzerland. In this case, it is apparent that, due to the high order parameter, the shift estimation can be unambiguously performed only in the crevasse area.

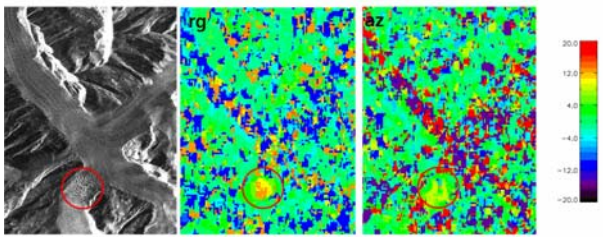

Figure 7. SAR image and shift maps from the Aletsch glacier, Switzerland

As far as the SNR is concerned, the simulation results show that if the minimum requirements on the texture characteristics are satisfied, the shift estimation is made unfeasible by the SNR only if it is lower than 0 dB (the noise power is greater than the signal power).

4.3. Very Fast Glaciers

Special attention deserves the case of very fast flowing glaciers, for which a first analysis has been carried out in [10].

In this case, the hypothesis of a uniform shift field within the patch does not hold anymore. A more realistic model for the shift field would consider a simple spatial variation of it, for which the first-order spatial derivatives are constant and the higher order spatial derivatives of the shift field are equal to zero.

For a given set of texture parameters, the value of the measure of similarity between the reference patch and the matching patch decreases, as the values of the first-order spatial derivatives of the shift field increase. When the values of those derivatives are significant, in fact, not only does the matching patch differ from the reference one in the residual speckle pattern, but also in its underlying RCS, which can be seen as a stretched version of the RCS of the reference patch. In contrast, when the values of the first-order derivatives of the shift field are close to zero, the two patches only differ because of the residual speckle and their correlation is expected to be rather high.

In order to understand how high the values of those derivatives can be, simulations have been run. The first-order derivatives of the shift field have been assumed to be constant within the patch, while higher order derivatives have been assumed to be null. Fig. 8 shows the PDFs of the cross-correlation coefficient between matching patches (dashed line) and between non-matching patches (solid lines), for different values of the first-order spatial derivatives of the shift field in a particular case study, where all the other parameters have been fixed. As the values of the derivatives increase, the expected value of the cross-correlation between matching-patches decreases.

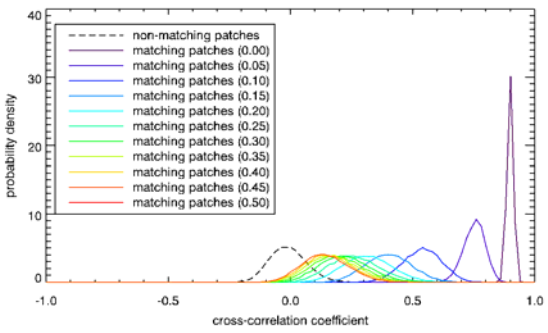

Figure 8. SAR image and shift maps from the Aletsch glacier, Switzerland

In order to keep low the number of wrong estimates, in this special case, the values of the derivatives should not exceed 0.1, i.e. the difference of the shifts of two neighboring pixels has to be smaller than 0.1 pixels. As long as the failures are few and sparse, in fact, they can be identified and the correct shift can be retrieved by means of post-processing.

For a given glacier and a short observation period, the shift field can be assumed to be proportional to the temporal baseline and so are their derivatives. This analysis is helpful to select the repeat cycle for a mission, whose aim is to monitor fast-flowing glaciers.

5. ACCURACY OF THE SHIFT ESTIMATION

5.1. Monte Carlo Simulations

The estimation accuracy is complicate to be derived analytically. However, once the image and processing parameters are given, it can be evaluated by means of Monte Carlo simulations.

The method consists of generating the two dimensional underlying RCS trend (N_{rg} X N_{az} pixels) according to the desired statistics, duplicating this RCS trend and multiplying them by two uncorrelated speckle patterns, adding the thermal noise, then performing the described processing and estimating the shift. This is repeated for a very large number of trials (a different RCS trend is generated for each trial, but all are characterized by the same texture parameters), so that statistics of the estimated shift can be obtained. As the real value of the shift is zero, the estimated shift corresponds to the estimation error and its standard deviation to the accuracy of the differential shift estimation.

Fig. 9 shows the distribution of the estimation error for a given set of parameters as obtained by Monte-Carlo simulations, using NCC and ML. The latter similarity function leads to better estimation accuracy.

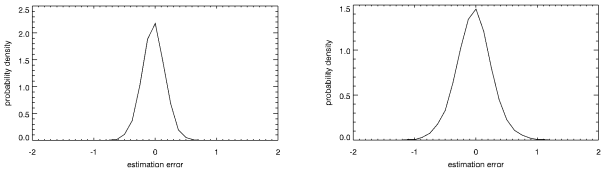

Figure 9. PDF of the estimation error, using NCC (left) and ML (right)

5.2. Impact of Despeckling

The dependence of the estimation accuracy on the despeckling window size is depicted in Fig. 10 for different order parameters.

As apparent, the estimation of the differential shift without performing any despeckling is characterized by a degraded accuracy.

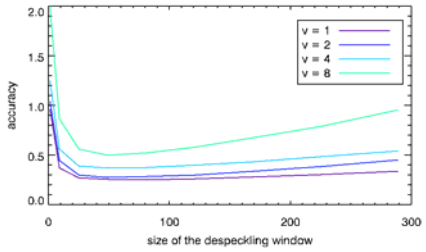

Figure 10. PDF of the estimation error, using NCC (left) and ML (right)

5.3. Number of Resolution Cells Used for the Shift Estimation

When the mutual shift of image elements is estimated by means of coherent cross-correlation, in the presence of partial coherence, the accuracy of the shift estimation is in inverse proportion to the square root of the number of resolution cells [2][3].

Despeckled intensity images, used for feature-tracking, are not characterized by statistical independence of the values of adjacent resolution cells. Monte Carlo simulations show that the above mentioned relation between standard deviation of the estimation error and size of the patches used for the estimation still holds.

Furthermore, the standard deviation of the estimation error is also independent of the shape of the patches used for the estimation (the same accuracy is achieved by using either 64 X 64 or 128 X 32 patches), holding:

$$\sigma_{rg} \propto \frac{1}{\sqrt{N_{rg} N_{az}}}; \qquad \sigma_{az} \propto \frac{1}{\sqrt{N_{rg} N_{az}}} \tag{10}$$

It is important to recall that the formula, valid for both the NCC and the ML similarity functions, holds as long as all the cells used for the estimation are characterized by the same range and azimuth shift.

5.4. Texture Parameters and SNR

Fig. 11 shows the accuracy of the shift estimation as a function of the order parameter for different values of the correlation lengths, assumed to be equal in the range and azimuth direction, using NCC and ML. They are useful to figure out the achievable accuracy of this technique. For a 64 X 64 patch size, the accuracy of the shift estimation ranges from 0.2 to 1.2 resolution cell, depending on the texture parameters. According to (10), for a 128 X 128 patch size, the accuracy halves. In case the range and azimuth correlation lengths and/or the range and azimuth resolution are not equal, the accuracy of the range shift estimation differs from the accuracy of

the azimuth shift estimation. It is important to remark that, according to the simulations, ML performs better than NCC.

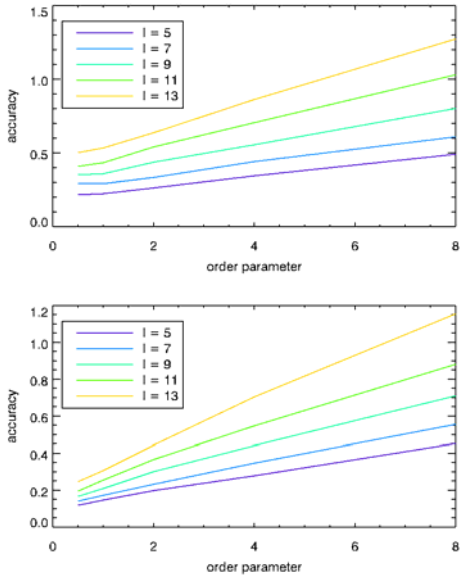

Figure 11. Accuracy of the shift estimation using NCC (top) and ML (bottom)

Fig. 12 shows the trend of the accuracy of the shift estimation as a function of the SNR. It is apparent that, for values of SNR is greater than 8 dB, the performance improvement is very small. It is also interesting to notice that, for very low values of SNR, NCC performs better than ML. This is not surprising, because for low values of SNR, the effect of the additive thermal noise dominates over the effect of the multiplicative noise (speckle).

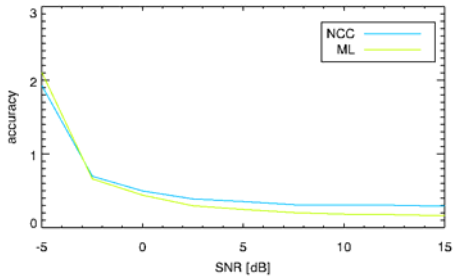

Figure 12. Accuracy of the shift estimation vs. SNR

5.5. Very fast glaciers

A non-uniform shift field between the two patches affects the accuracy of the shift estimation. Fig. 13 shows how the accuracy degrades with increasing values of the first-order derivatives of the shift field, assuming that they are constant and that the higher order spatial derivatives of the shift field are equal to zero. It is noticeable that for a non-uniform shift field, a larger patch does not necessary lead to better accuracy. This is due to the fact that the matching patch differs from the reference one not only in the residual speckle pattern, but also in its underlying RCS.

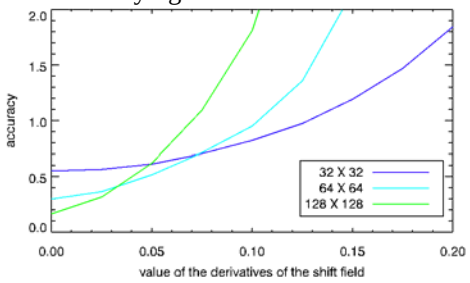

Figure 13. Accuracy for very fast glaciers

6. BENEFITS OF POLARIMETRY

6.1. Selection of the Most Suited Polarisation

Feature-tracking can benefit of the availability of fully-polarimetric data. Some texture characteristics, such as the order parameter, are polarization-dependent. The choice of the optimum polarisation may therefore lead to improved performance.

In case fully-polarimetric data are available, for each pixel of the image, a three-element complex vector is available. Let us assume that the information related to the different channels is collected in the Pauli vector:

$$\mathbf{k_P} = \left[S_{hh} + S_{vv} \quad S_{hh} - S_{vv} \quad 2S_{hv}\right]^T \qquad (11)$$

An arbitrary polarisation can be selected by multiplying the transpose scattering mechanism vector **w** [11], a unit modulus vector made up of five independent parameters, by the Pauli vector. In order to select a polarisation, in fact, we have to choose three complex coefficients or six real parameters, one of which is dependent on the others, as the vector has unit modulus. In effect, as we are only interested in the intensity of the image so obtained, we don't need to specify the phases of the all three complex coefficient, but it is enough to specify two of them, therefore only four independent parameters have to be specified:

$$\mathbf{w} = \left[\cos\alpha \quad \sin\alpha\cos\psi\exp(j\phi_1) \quad \sin\alpha\sin\psi\exp(j\phi_2)\right]^T \qquad (12)$$

By varying these parameters, it is possible to explore the entire space of polarisations. In particular, for a patch taken from the crevasses area of the Aletsch glacier, Switzerland, the order parameter has been evaluated for all the possible polarisations. The order parameter ranges from 1.25 to 2.75, being 1.75 the average order parameter. The performance improvement can be inferred from the plots of Fig. 11. The standard deviation of the estimation error for an order parameter of 2.75 is approximately twice as large as the standard deviation for an order parameter of 1.25.

6.2. Filtering the Speckle in the Polarimetric Domain

An as alternative, fully-polarimetric data can be exploited by performing some despeckling in the polarimetric domain. Polarimetric Whitening Filter (PWF) combines the three complex elements S_{hh}, S_{vv}, and S_{hv} of the polarimetric scattering matrix to reduce speckle [12]. A model for the clutter covariance matrix is assumed, being the elements of this matrix adaptively estimated from local data. In this case only some components of the covariance matrix are used to obtain the despeckled image. More sophisticated speckle filters, reviewed in [13], allow the filtering of the entire covariance matrix, so preserving the statistical characteristics of the data, but we are not aware of a method to use all the polarimetric information (including the phases) for feature-tracking, given our hypothesis of absence of coherence.
Fig. 14 shows the improvement in the estimation accuracy achieved in the presence of fully-polarimetric data, keeping constant the resolution and assuming that the equivalent number of looks of the despeckling operation in the polarimetric domain is equal to three.

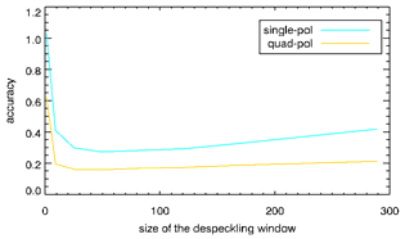

Figure 14. Accuracy using fully-polarimetric data

7. CONCLUSIONS

Feature-tracking has been dealt with throughout the paper, with special attention to the dependence of the performance on image and processing parameters.
The analysis has shown that despeckling of the images before estimating the differential shift reduces the number of wrong estimates and leads to more accurate shift estimation.
The feasibility requirements are mainly related to the presence of features, i.e. the order parameter of the texture should be not greater than 8, but also to the temporal baseline between consecutive observations, when dealing with very-fast glaciers.
As far as the accuracy of the shift estimation is concerned, this is strongly dependent on the size of the patches used for the estimation, or better on the number of pixels for which the difference between differential shifts does not exceed the correlation length of the textures. For patch sizes of 64 X 64 or 128 X 128 resolution cells, likely to be used for glacier monitoring applications, accuracies up to a tenth of a resolution cell are achievable. Further improvements are achieved, in case fully polarimetric data are available.
Feature-tracking is effective to monitor fast-flowing glaciers, when coherence between consecutive acquisitions is not likely to be retained.
The analysis performed, however, is applicable to applications other than glacier monitoring.

REFERENCES

1. Short N.H. & Gray A.L. (2004). Potential for RADARSAT-interferometry: glacier monitoring using speckle tracking. Can. J. Remote Sensing. **30 (**3), 504-509.
2. Bamler R. & Eineder M. (2005). Accuracy of Differential Shift Estimation by Correlation and Split-Bandwidth Interferometry for Wideband and Delta-k SAR Systems. IEEE Geo. and Rem. Sens. Lett. **2** (2), 151-155.
3. Bamler R. (2000). Interferometric Stereo Radargrammetry: Absolute Height Determination from ERS-ENVISAT Interferograms. In *Proc. IGARSS*, vol. 2, pp742-725.
4. Oliver C. & Quegan S. (1998). *Understanding Synthetic Aperture Radar Images*, Artech House, London, UK.
5. López Martinez C. (2003). *Multidimensional Speckle Noise. Modelling and Filtering Related to SAR Data*. PhD Thesis.
6. Blacknell D., Blake A., Lombardo P. & Oliver C.. (1994). A Comparison of Simulation Techniques for Correlated Gamma and K-Distributed Images for SAR Applications. In *Proc. IGARSS*, vol. 4, pp2182-2184.
7. Armstrong B. C. & Griffiths H. D. (1991). Modelling Spatially-Correlated K-Distributed Clutter. Elect. Lett. **27**(15), 1355-1356.
8. Lombardo P. & Oliver C. J. (1994). Estimation of texture parameters in K-distributed clutter. IEE Proc. Radar, Sonar, Navig. **141**(4), 196-204.
9. Erten E., Reigber A., Hellwich O. & Prats P. (2009). Glacier Velocity Monitoring by Maximum Likelihood Texture Tracking. IEEE Trans. Geo. and Rem. Sens. **47**(2), 394-405.
10. Villano M., Moreira A., Miller H., Rott H., Hajnsek I., Bamler R., López-Dekker P., Börner T., De Zan F., Krieger G. & Papathanassiou K.P. (2010). SIGNAL: Mission Concept and Performance Assessment. In *Proceedings of the 8th European Conference on Synthetic Aperture Radar (EUSAR)*, Aachen, Germany, 7-10 June 2010, pp520-523.
11. Cloude S. (2009). *Polarisation: Application in Remote Sensing*, Oxford University Press.
12. Novak N.L. & Burl M.C. (1990). Optimal speckle reduction in polarimetric SAR imagery. IEEE Trans. Aerospace Electron. Sys. **26**, 293-305.
13. Lee J.S. & Pottier E. (2009). *Polarimetric Radar Imaging: From Basics to Applications*, CRC Press.